J. Fluid Mech. (2014), *vol.* 743, *pp.* 280–294.
doi:10.1017/jfm.2014.29

Damping of inertial motions by parametric subharmonic instability in baroclinic currents

Leif N. Thomas[1,†] **and John R. Taylor**[2]

[1]Department of Environmental Earth System Science, Stanford University, Stanford, CA 94305, USA

[2]Department of Applied Mathematics and Theoretical Physics, University of Cambridge, Centre for Mathematical Sciences, Wilberforce Road, Cambridge CB3 0WA, UK

(Received 19 July 2013; revised 11 November 2013; accepted 8 January 2014; first published online 4 March 2014)

A new damping mechanism for vertically-sheared inertial motions is described involving an inertia–gravity wave that oscillates at half the inertial frequency, f, and that grows at the expense of inertial shear. This parametric subharmonic instability forms in baroclinic, geostrophic currents where thermal wind shear, by reducing the potential vorticity of the fluid, allows inertia–gravity waves with frequencies less than f. A stability analysis and numerical simulations are used to study the instability criterion, energetics, and finite-amplitude behaviour of the instability. For a flow with uniform shear and stratification, parametric subharmonic instability develops when the Richardson number of the geostrophic current nears $Ri_{PSI} = 4/3 + \gamma \cos\phi$, where γ is the ratio of the inertial to thermal wind shear magnitude and ϕ is the angle between the inertial and thermal wind shears at the initial time. Inertial shear enters the instability criterion because it can also modify the potential vorticity and hence the minimum frequency of inertia–gravity waves. When this criterion is met, inertia–gravity waves with a frequency $f/2$ and with flow parallel to isopycnals amplify, extracting kinetic energy from the inertial shear through shear production. The solutions of the numerical simulations are consistent with these predictions and additionally show that finite-amplitude parametric subharmonic instability both damps inertial shear and is itself damped by secondary shear instabilities. In this way, parametric subharmonic instability opens a pathway to turbulence where kinetic energy in inertial shear is transferred to small scales and dissipated.

Key words: baroclinic flows, internal waves, parametric instability

1. Introduction

A large fraction of the kinetic energy in the ocean's inertia–gravity wave spectrum is contained in inertial motions (Ferrari & Wunsch 2009). These motions are primarily generated by wind forcing, resulting in oscillatory currents with a frequency equal to the local Coriolis parameter, $f = 2\Omega \sin\lambda$, where Ω is the angular velocity of the Earth and λ is the latitude. While the generation mechanisms of inertial motions are relatively well-understood, the manner in which their kinetic energy is lost is less certain. Various damping mechanisms have been proposed, including shear instability

† Email address for correspondence: leift@stanford.edu

(Alford & Gregg 2001), wave absorption in critical layers (Kunze, Schmitt & Toole 1995), and energy transfer via wave–wave interactions (Müller *et al.* 1986). One wave–wave interaction is parametric subharmonic instability, which leads to the transfer of energy from a wave of a given frequency to its subharmonic at half the frequency. In principle, using classical inertia–gravity wave theory, parametric subharmonic instability can be ruled out as a local damping mechanism for inertial motions because the classical dispersion relation does not allow for freely-propagating waves of frequency $f/2$. Non-locally though, near-inertial waves that propagate equatorward, and hence become superinertial, can undergo parametric subharmonic instability when they reach the latitude where the local inertial frequency is half their frequency (Nagasawa, Niwa & Hibiya 2000).

The classical dispersion relation does not, however, take into consideration background flows that can change the range of permissible frequencies for propagating inertia–gravity waves. A more general expression for the minimum frequency of inertia–gravity waves in a unidirectional current $\overline{u}(y, z)$ and density field $\overline{\rho}(y, z)$ is

$$\sigma_{min} = \sqrt{\frac{fq}{N^2}}, \tag{1.1}$$

where $q = (f - \partial\overline{u}/\partial y)N^2 + (\partial\overline{u}/\partial z)(\partial\overline{b}/\partial y)$ is the Ertel potential vorticity, y and z are the coordinates perpendicular to the current in the horizontal and vertical directions, respectively, $\overline{b} = -g\overline{\rho}/\rho_o$ is the buoyancy (g is the acceleration due to gravity and ρ_o is a reference density used in the Boussinesq approximation), and $N = \sqrt{\partial\overline{b}/\partial z}$ is the buoyancy frequency which is assumed to be larger than f (Hoskins 1974; Whitt & Thomas 2013). When $N > f$, the waves of minimum frequency are those that drive fluid parcel displacements, (Y, Z), that follow density surfaces, i.e. $Z = -Y(\partial\overline{b}/\partial y)/N^2$, and thus lack a buoyancy force. For these motions the restoring force is purely ascribable to the Coriolis force, $-fu'$, where u' is the wave-induced velocity anomaly in the direction of the background current. Since the flow does not vary in this direction, in the inviscid limit, the absolute momentum, $u' + \overline{u} - fY$, is conserved and consequently, $u' = (f - \partial\overline{u}/\partial y)Y - (\partial\overline{u}/\partial z)Z$ for small displacements. When these displacements are constrained to density surfaces, the Coriolis force follows Hooke's law: $-fu' = -[f(f - \partial\overline{u}/\partial y) + f(\partial\overline{u}/\partial z)(\partial\overline{b}/\partial y)/N^2]Y$, resulting in oscillatory motions with frequency (1.1).

In the limit of no flow the potential vorticity simplifies to $q = fN^2$, and the classical result for the minimum frequency, $\sigma_{min} = f$, is recovered. However, in a baroclinic flow with a horizontal buoyancy gradient in hydrostatic and geostrophic balance with a 'thermal wind' shear $\partial\overline{u}/\partial z = -(\partial\overline{b}/\partial y)/f$, the minimum frequency is always reduced by baroclinicity, $\sigma_{min} = \sqrt{f(f + \partial\overline{u}/\partial y) - (\partial\overline{b}/\partial y)^2/N^2}$. It follows that for a sufficiently strong horizontal buoyancy gradient, the minimum frequency of inertia–gravity waves can be lowered to a value near $f/2$, suggesting that parametric subharmonic instability could grow locally from inertial motions. This mechanism could play an important role in dissipating wind-driven inertial currents at ocean fronts – highly baroclinic regions with strong lateral density gradients. In this article we explore this scenario using a combination of analytical theory and numerical simulation.

2. Analytical model

2.1. *Basic state*

A simple configuration is used to study the damping of inertial motions by parametric subharmonic instability in a baroclinic current. Specifically, we will consider an

unbounded domain and background buoyancy, $\overline{b}$, and flow fields, $(\overline{u}, \overline{v}, \overline{w})$, with spatially uniform gradients:

$$\overline{u} = \frac{S^2}{f} z + \breve{u}(t) z, \quad \overline{v} = \breve{v}(t) z, \quad \overline{w} = 0, \quad \overline{b} = N^2(t) z - S^2 y. \tag{2.1}$$

This basic state is in hydrostatic balance with a pressure field

$$\overline{p} = -\rho_o \left[S^2 y z - \tfrac{1}{2} N^2 z^2 \right]. \tag{2.2}$$

Since the geostrophic current needed to balance $\overline{p}$ is $(S^2/f)z$, the background flow departs from geostrophy by an amount set by $\breve{u}$ and $\breve{v}$, the *ageostrophic shear*. Substitution of (2.1) and (2.2) into the Boussinesq, inviscid, adiabatic equations of motion:

$$\frac{\mathrm{D}\boldsymbol{u}}{\mathrm{D}t} + f\hat{\boldsymbol{z}} \times \boldsymbol{u} = -\frac{1}{\rho_o} \nabla p + b\hat{\boldsymbol{z}}, \tag{2.3}$$

$$\frac{\mathrm{D}b}{\mathrm{D}t} = 0, \tag{2.4}$$

where $\mathrm{D}/\mathrm{D}t = \partial/\partial t + \boldsymbol{u} \cdot \nabla$ is the material derivative, results in a set of ordinary differential equations for the ageostrophic shear $(\breve{u}, \breve{v})$ and the stratification $N^2(t)$:

$$\frac{\partial \breve{u}}{\partial t} - f\breve{v} = 0, \tag{2.5}$$

$$\frac{\partial \breve{v}}{\partial t} + f\breve{u} = 0, \tag{2.6}$$

$$\frac{\partial N^2}{\partial t} = \breve{v} S^2. \tag{2.7}$$

For convenience, the ageostrophic shear can be written in terms of the geostrophic shear with a scaling factor γ so that the initial conditions are

$$N^2(t=0) = N_o^2, \quad \breve{u}(t=0) = \gamma \left(\frac{S^2}{f} \right) \cos\phi, \quad \breve{v}(t=0) = \gamma \left(\frac{S^2}{f} \right) \sin\phi, \tag{2.8}$$

where ϕ is the initial phase of the inertial oscillation. The background flow then satisfies the exact solution

$$\overline{u} = \frac{S^2}{f} z \left[1 + \gamma \cos(ft - \phi) \right], \tag{2.9}$$

$$\overline{v} = -\gamma \left(\frac{S^2}{f} \right) z \sin(ft - \phi), \tag{2.10}$$

$$N^2 = N_o^2 - \gamma \frac{S^4}{f^2} \left[\cos\phi - \cos(ft - \phi) \right]. \tag{2.11}$$

This basic state is a superposition of an inertial oscillation and an idealization of a front with a vertically-sheared geostrophic flow. Similar to other studies of fronts (e.g. Hoskins 1982), we assume that variations of the variables in the along-front, x, direction are much weaker than those in the cross-front, y, direction, and set them explicitly equal to zero in the analysis. Changes in stratification are caused by the cross-front component of the inertial shear which differentially advects buoyancy, e.g. (2.7). Since the flow is inviscid and adiabatic, the potential vorticity is conserved, i.e. $\mathrm{D}q/\mathrm{D}t = 0$. Thus, while the stratification of the background flow changes in time, its

potential vorticity is constant and equal to:

$$\overline{q} = fN^2 + \frac{\partial \overline{u}}{\partial z}\frac{\partial \overline{b}}{\partial y} = fN_o^2 - \frac{S^4}{f}(1 + \gamma \cos\phi). \tag{2.12}$$

It is important to note that at a front, the presence of a vertically-sheared inertial oscillation can modify the potential vorticity relative to an undisturbed balanced state. The reason for this is that the horizontal component of the vorticity associated with the oscillation can project into the horizontal buoyancy gradient of the front. How large a contribution this is depends on the strength of the inertial shear (i.e. γ) and the phase of the oscillation ϕ. If at $t = 0$ the inertial shear is entirely in the down-front direction, i.e. $\phi = 0$, then the potential vorticity is reduced relative to the case with no inertial oscillation since the inertial and thermal wind shears add; the opposite is true if the inertial shear is up-front ($\phi = \pi$) at $t = 0$. When the inertial shear is entirely cross-front at $t = 0$, i.e. $\phi = \pi/2$, the potential vorticity is unaffected by the oscillation.

Given the potential vorticity (2.12), the time-mean stratification $\overline{N^2}^t = N_o^2 - (S^4/f^2)\gamma \cos\phi$, and the expression for the minimum frequency of inertia–gravity waves, (1.1), we may suppose heuristically that the first subharmonic of the inertial frequency can exist in this background flow when

$$\sqrt{\frac{f\overline{q}}{\overline{N^2}^t}} = \frac{f}{2}, \tag{2.13}$$

or, in terms of the Richardson number of the geostrophic flow,

$$Ri_{b,o} \equiv \frac{N_o^2 f^2}{S^4}, \tag{2.14}$$

when

$$Ri_{b,o} = Ri_{PSI} = \tfrac{4}{3} + \gamma \cos\phi. \tag{2.15}$$

Note that this result can be derived formally using a parcel argument (not included here for brevity) that assumes along-isopycnal fluid parcel displacements and weak inertial shears, i.e. $\gamma \ll 1$. The implication of the above equations is that a parametric subharmonic instability can develop in baroclinic, geostrophic currents that are exposed to inertial shear when the Richardson number of those currents satisfies the criterion (2.15). In the next section we test this prediction using a model for the evolution of plane-wave perturbations to the basic state.

2.2. *Stability analysis*

The basic state described by (2.1) and (2.2) is perturbed with a two-dimensional (i.e. invariant in the x-direction) disturbance, with velocity, buoyancy, and pressure fields $\boldsymbol{u}'(y, z, t)$, $b'(y, z, t)$, and $p'(y, z, t)$. The dynamics of the perturbations are governed by the incompressible, Boussinesq equations:

$$\frac{\mathrm{D}\boldsymbol{u}'}{\mathrm{D}t} + \boldsymbol{u}' \cdot \nabla \overline{\boldsymbol{u}} + \boldsymbol{u}' \cdot \nabla \boldsymbol{u}' + f\hat{\boldsymbol{z}} \times \boldsymbol{u}' = -\frac{1}{\rho_o}\nabla p' + b'\hat{\boldsymbol{z}}, \tag{2.16}$$

$$\frac{\mathrm{D}b'}{\mathrm{D}t} + \boldsymbol{u}' \cdot \nabla \overline{b} + \boldsymbol{u}' \cdot \nabla b' = 0, \tag{2.17}$$

$$\nabla \cdot \boldsymbol{u}' = 0, \tag{2.18}$$

where $\mathrm{D}/\mathrm{D}t = \partial/\partial t + \overline{v}\partial/\partial y$ is the rate of change following the background flow. Since the perturbations are two-dimensional, the flow in the y–z plane can be expressed in terms of a streamfunction, i.e. $v' = \partial\psi/\partial z$, $w' = -\partial\psi/\partial y$. Due to the lack of boundaries, and to the spatially-uniform gradients of the basic state, the method of Craik (1989) can be employed, i.e. solutions in the form of plane waves

$$\begin{bmatrix} u' \\ \psi \\ b' \\ p' \end{bmatrix} = \begin{bmatrix} U(t) \\ \Psi(t) \\ B(t) \\ P(t) \end{bmatrix} \mathrm{e}^{\mathrm{i}\varphi} + \text{c.c.}, \tag{2.19}$$

are sought, where $\varphi = ly + mz$ is the phase and $\boldsymbol{k} = (l, m)$ is the wavevector which is spatially uniform, yet varies with time. Here, the evolution of a single plane wave is considered, which makes the nonlinear terms in (2.16)–(2.17) identically equal to zero. In the next section, numerical simulations will consider more general perturbations. With the ansatz (2.19) it follows that the phase does not change following the background flow, i.e. $\mathrm{D}\varphi/\mathrm{D}t = 0$, yielding the following solution for the wavevector:

$$l = l_o, \quad m = m_o + \gamma\frac{S^2}{f^2}\left[\cos\phi - \cos(ft - \phi)\right] l_o, \tag{2.20}$$

where (l_o, m_o) denotes its initial value. The slope of streamlines, $-l/m$, which sets the direction of the velocity vector in the y–z plane, can be computed from (2.20). When the initial slopes of isopycnals and streamlines are equal, i.e.

$$\frac{l_o}{m_o} = -\frac{S^2}{N_o^2}, \tag{2.21}$$

isolines of the two fields remain parallel for all times (compare (2.11) and (2.20)). Perturbations with this wavevector have flow that is purely along isopycnals and thus should yield oscillatory motions with the lowest frequency due to a lack of buoyancy forces. They should thus be the first perturbations to grow via parametric subharmonic instability when $Ri_{b,o}$ is lowered to the critical value (2.15). Consequently we will only consider plane waves that satisfy constraint (2.21) in the stability analysis, but will make no such restriction in the numerical simulations, allowing us to test the theoretical prediction.

Substituting the ansatz (2.19) into (2.16)–(2.18), using constraint (2.21), which implies that $b' = 0$ for all times, and deriving a streamwise vorticity equation to eliminate pressure, yields a set of two coupled ordinary differential equations for the amplitude of the plane-wave disturbance $\boldsymbol{a} = [U\ \Psi]^T$:

$$\dot{\boldsymbol{a}} = \boldsymbol{E}(t)\boldsymbol{a}, \tag{2.22}$$

where the overdot denotes a time derivative and the matrix $\boldsymbol{E}$ has the elements

$$\left.\begin{aligned} &\boldsymbol{E}_{11} = 0 \quad \boldsymbol{E}_{12} = \mathrm{i}fm + \mathrm{i}\frac{S^2}{f}[1 + \gamma\cos(ft - \phi)]l \\ &\boldsymbol{E}_{21} = \mathrm{i}mf|\boldsymbol{k}|^{-2} \quad \boldsymbol{E}_{22} = -(|\dot{\boldsymbol{k}}|^2)|\boldsymbol{k}|^{-2}. \end{aligned}\right\} \tag{2.23}$$

These ordinary differential equations were solved numerically as an initial-value problem for a range of background flow parameters, $Ri_{b,o}$, γ, and ϕ. A regime diagram highlighting the regions where perturbations grow in the space spanned by these three parameters is shown in figure 1. To rule out symmetric instability

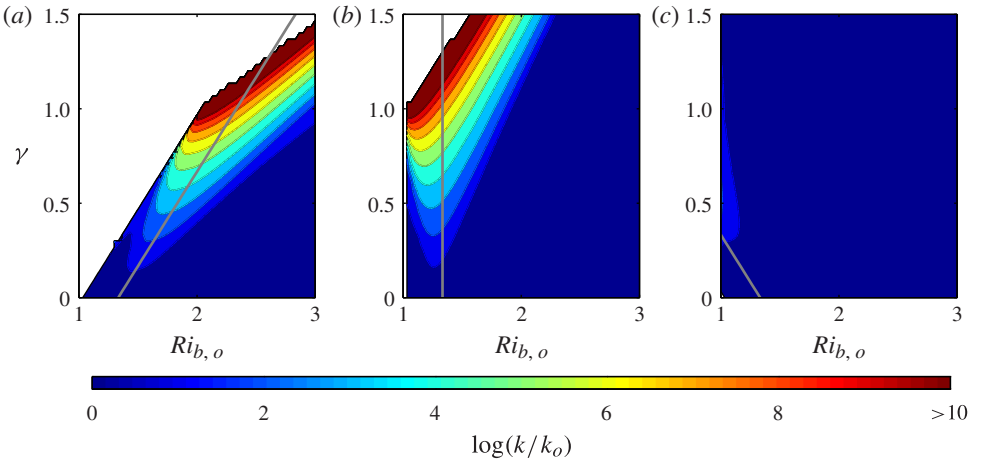

FIGURE 1. Regime diagram illustrating the locations in the parameter space $Ri_{b,o}$–γ where parametric subharmonic instability occurs for an inertial shear that is initially directed (*a*) down-front ($\phi = 0$), (*b*) across-front ($\phi = \pi/2$) and (*c*) up-front ($\phi = \pi$). The prediction for the critical Richardson number for parametric subharmonic instability, Ri_{PSI} (2.15), is denoted by the grey line. The colour shading is the logarithm of the perturbation kinetic energy normalized by its initial value, k_o, and evaluated at four inertial periods for flow perturbations that are purely isopycnal and satisfy (2.21). The part of parameter space where the background flow is unstable to symmetric instability or Kelvin–Helmholtz instability (i.e. where the potential vorticity of the background flow is less than zero and/or where the minimum value of the Richardson number of the background flow is less than 0.25) has been left blank.

and Kelvin–Helmholtz instability we only consider background flows with positive potential vorticity and gradient Richardson numbers $\overline{Ri} = N^2/|\partial\overline{\boldsymbol{u}}/\partial z|^2 > 1/4$. Despite these constraints, growing modes exist that occupy regions in parameter space that are centred about the prediction for the critical Richardson number for parametric subharmonic instability, i.e. Ri_{PSI} (2.15). The growth of the instabilities is strongly dependent on the initial direction of the inertial shear relative to the thermal wind shear. In particular, a background flow that is unstable for an inertial shear that is initially in the direction of the thermal wind shear (i.e. down-front with $\phi = 0$) can be stable for an initial inertial shear in the opposite direction. This is fundamentally due to the modification of the potential vorticity by inertial shear, e.g. (2.12), and its effect on the minimum frequency of inertia–gravity waves.

In this calculation m and N^2 are specified at $t = 0$ and results are presented for various values of ϕ. This is one approach that emphasizes the importance of the modification of the potential vorticity by the inertial motions and its effect on the instability. Perhaps a more common approach for time-periodic flows would be to consider fixed average values of m and N^2 over the periodic cycle; in this case, the results would be independent of ϕ. This does not imply any contradiction with the present results, but merely a different manner of presentation of the same results. However, in making the time-mean value of N^2 invariant with ϕ, the stratification in the absence of inertial motions, N_o^2, has to be adjusted to compensate for the modification of the potential vorticity by the inertial shear, which is not the physical application that we have in mind.

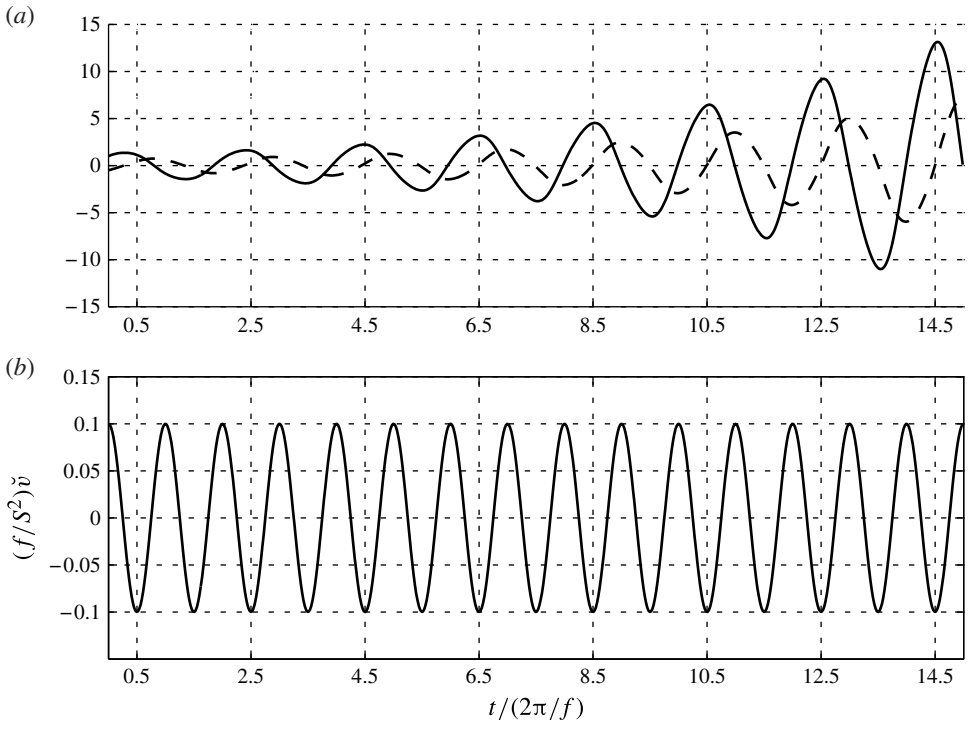

FIGURE 2. Example solution illustrating parametric subharmonic instability for $\gamma = 0.1$, $Ri_{b,o} = 4/3$, $\phi = \pi/2$, and $l_o/m_o = -S^2/N_o^2 = 0.013$ obtained by solving (2.22) numerically. (*a*) The perturbation to the along- and across-front velocity, u' and v' (dashed and solid lines, respectively) normalized by the initial value of the across-front velocity, v'_o. (*b*) The vertical shear of the across-front flow of the basic state, $\partial\overline{v}/\partial z$, normalized by the thermal wind shear. Time is non-dimensionalized in terms of inertial periods.

The underlying physics behind the growing modes apparent in figure 1 can be illustrated using an example solution, as shown in figure 2. For this example the Richardson number of the geostrophic flow satisfies criterion (2.15) and, as predicted, the perturbations are characterized by waves that oscillate at half the inertial frequency but that grow in amplitude. The amplitudes of the along- and across-front perturbation velocity (u' and v', respectively) are not equal, consistent with the polarization relations of subinertial inertia–gravity waves in a unidirectional, baroclinic current (Whitt & Thomas 2013). Figure 2 also reveals the particular phase relation between the perturbation and the inertial oscillation, namely $v' = 0$ when $\partial\overline{v}/\partial z$ nears its maximum. This phase relation is essential to the growth mechanism of parametric subharmonic instability and can be understood in terms of the energetics of the perturbations.

The energetics of the perturbations is governed by the following equation:

$$\frac{\mathrm{D}}{\mathrm{D}t}k = \underbrace{-\overline{u'w'}\frac{S^2}{f}}_{GSP} \underbrace{-\overline{v'w'}\breve{v} - \overline{u'w'}\breve{u}}_{AGSP} \underbrace{-\nabla\cdot\overline{\boldsymbol{u}'p'}}_{PWORK} + \underbrace{\overline{w'b'}}_{BFLUX}, \tag{2.24}$$

where $k = (1/2)\overline{\boldsymbol{u}'\cdot\boldsymbol{u}'}$ is the perturbation kinetic energy, averaged in the y–z plane. In general, k can be changed by convergences/divergences of the energy flux (*PWORK*)

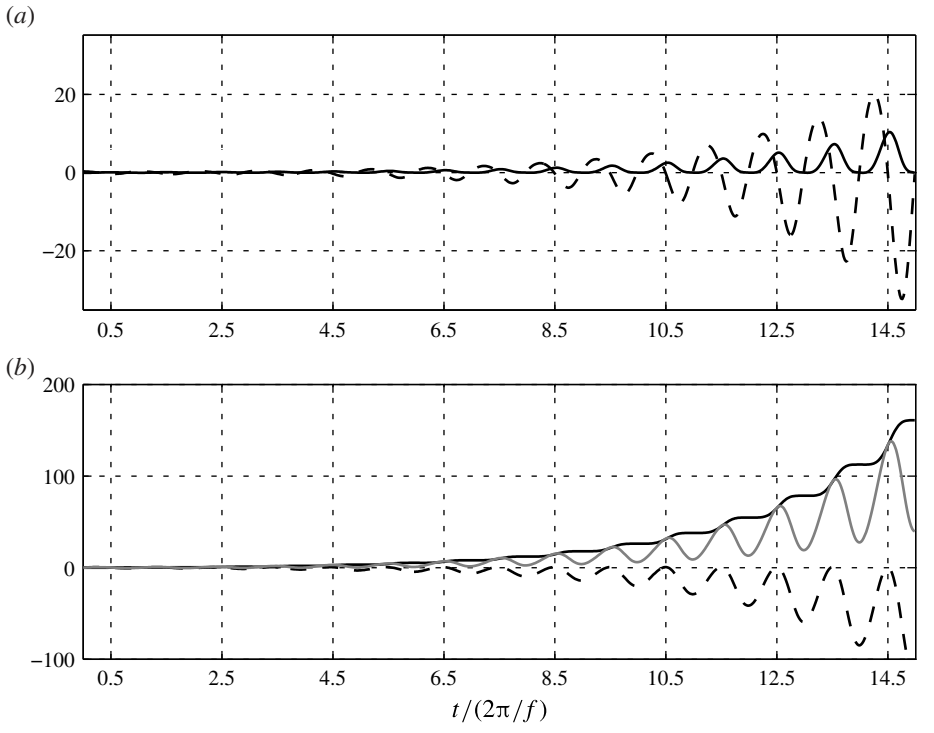

FIGURE 3. Terms in the perturbation kinetic energy equation (2.24) and their time integrals for the example solution illustrating parametric subharmonic instability shown in figure 2. (*a*) The shear production terms non-dimensionalized by the initial kinetic energy of the perturbation, k_o, and f, i.e. $AGSP/(2fk_o)$ (solid) and $GSP/(2fk_o)$ (dashed). (*b*) The total change in kinetic energy of the perturbation, $(k-k_o)/k_o$ (solid grey) and that attributable to ageostrophic and geostrophic shear production, i.e. $\int_0^t (AGSP/k_o)\mathrm{d}t'$ (solid black) and $\int_0^t (GSP/k_o)\mathrm{d}t'$ (dashed black).

and the release of potential energy via the buoyancy flux (*BFLUX*). However, for perturbations with no buoyancy anomaly that we consider, $BFLUX = 0$ and the divergence of the mean energy flux (*PWORK*) is negligibly small. The disturbances can also exchange kinetic energy with the background flow through shear production. The shear production can be decomposed into its geostrophic and ageostrophic parts (*GSP* and *AGSP* respectively) with the latter representing the rate of kinetic energy extraction from the inertial oscillation.

The two shear production terms were evaluated using the solution shown in figure 2 and are presented in figure 3(*a*). Both terms oscillate in time yet have biases. On average, *AGSP* is positive while *GSP* is negative. The change in kinetic energy caused by the two shear production terms can be quantified by taking their time integrals. As shown in figure 3(*b*), the kinetic energy increase by the *AGSP* outweighs the decrease by the *GSP*, resulting in a net growth of the perturbations. Thus the waves gain kinetic energy at the expense of the inertial oscillation.

The *AGSP* is on average positive in spite of the changing sign of the oscillatory background shear because of the phase relation between the inertial shear and the vertical flux of across-front momentum. This momentum flux, $\overline{v'w'}$, is positive definite because the perturbation velocity is constrained to run along isopycnals, e.g. (2.21),

$Ri_{b,o}$	ϕ	L/H	N_o/f	S/f	γ	q/f^3	$Re = U_0H/\nu$	$Pe = U_0H/\kappa$
1.65	0	15	75.9	7.7	0.6	175	1.3×10^6	1.3×10^6
1.80	0	15	79.3	7.7	0.6	698	1.3×10^6	1.3×10^6
1.91	**0**	**15**	**81.7**	**7.7**	**0.6**	**1089**	$\mathbf{1.3 \times 10^6}$	$\mathbf{1.3 \times 10^6}$
2.00	0	15	83.5	7.7	0.6	1395	1.3×10^6	1.3×10^6
1.91	π	15	81.7	7.7	0.6	5277	1.3×10^6	1.3×10^6

TABLE 1. Non-dimensional simulation parameters. The parameter values in bold correspond to the simulation shown in figures 4–6. The Reynolds and Péclet numbers are calculated using the maximum initial ageostrophic velocity, $U_0 \equiv S^2 f^{-1} \gamma H$.

which slope upwards for this background flow. Consequently, the perturbations gain (lose) kinetic energy via the *AGSP* during periods when $\partial\overline{v}/\partial z < 0$ ($\partial\overline{v}/\partial z > 0$). The vertical flux of across-front momentum scales with $|\Psi|^2$, and is therefore minimum when $\Psi = 0$ and hence $v' = 0$. Since the frequency of the perturbation is half the inertial frequency, by timing the zeros in Ψ and v' with the maxima in $\partial\overline{v}/\partial z$ (as illustrated in figure 2), the perturbations minimize the loss of kinetic energy via the *AGSP* and maximize the extraction of kinetic energy from the inertial oscillation.

While the waves extract kinetic energy from the inertial motions, part of this kinetic energy is transferred to the geostrophic flow via the *GSP*. The net result is an exchange of kinetic energy from an unbalanced flow (an inertial oscillation) to a balanced flow (a baroclinic geostrophic current) with parametric subharmonic instability acting as the conduit for the energy transfer. This is in stark contrast to symmetric instability which derives its kinetic energy from the geostrophic flow via the *GSP* (Thomas & Taylor 2010).

3. Numerical simulations

3.1. *Setup*

To complement the stability analysis described above, we ran numerical simulations of the fully-nonlinear, incompressible Boussinesq equations. The simulations have two primary objectives: to test the predictions of the theory, and to explore the equilibration of the instability through nonlinear dynamics. Like the stability analysis above, the simulations are restricted to a two-dimensional plane, allowing for velocity in all three directions, while assuming that all flow variables are independent of the along-front (x) direction. However, while the stability analysis considered a single along-isopycnal mode, the simulations are initialized with random perturbations to the velocity field. This more general initial condition allows us to test the theoretical prediction that an along-isopycnal disturbance will emerge as the most unstable mode.

Table 1 lists the non-dimensional parameters used in each simulation. The parameters ($S = 7.7f$, $\gamma = 0.6$) were chosen to represent a relatively strong ocean front such as the Gulf Stream, with intense ageostrophic shear. Note that the potential vorticity is positive in all simulations, which implies that the flow will be stable to convective and symmetric instability. Periodic boundary conditions are applied to all fields in the horizontal direction, after subtracting a background horizontal density gradient. This makes these simulations very similar to the 'frontal zone' configuration used by several previous studies (Taylor & Ferrari 2009; Thomas & Taylor 2010; Taylor & Ferrari 2010). Free-slip boundary conditions are imposed at the top and bottom of the domain ($\partial u/\partial z = \partial v/\partial z = 0$, $w = 0$ at $z = 0, -H$) with a buoyancy

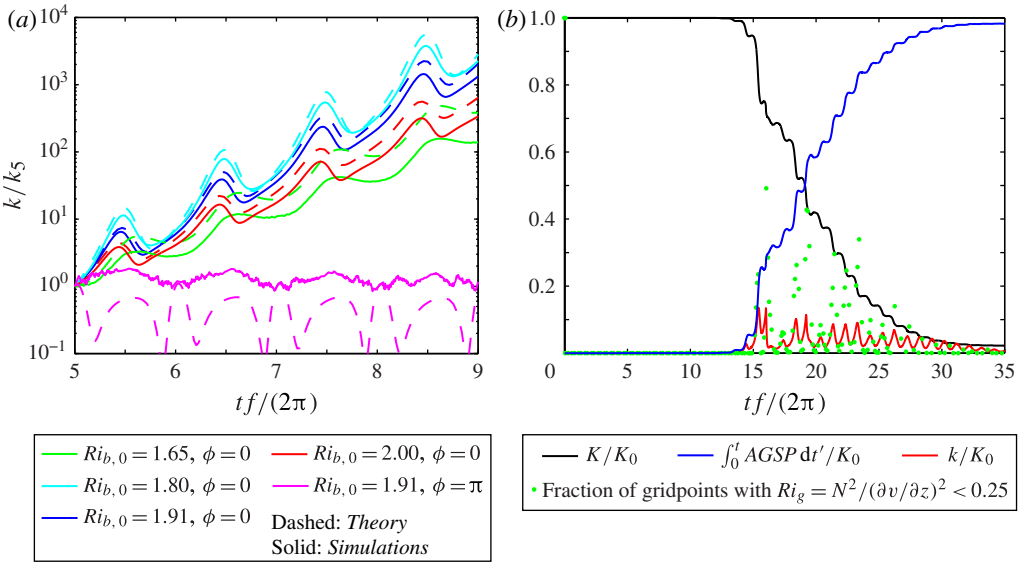

FIGURE 4. (*a*) Time series of the perturbation kinetic energy (k), normalized by the value at $tf/(2\pi) = 5$ (k_5) for the numerical simulations (solid) and theory (dashed) for the parameters listed in table 1. (*b*) Time series of the kinetic energy associated with the ageostrophic shear (black), time-integrated ageostrophic shear production (blue), and the perturbation kinetic energy (red) for the simulation highlighted in bold in table 1. Each of these terms has been normalized by the initial value of the kinetic energy associated with the ageostrophic shear, K_o. Green dots indicate the fraction of gridpoints where the gradient Richardson number is less than 0.25. Note that only the cross-front shear is used to calculate the gradient Richardson number since potential shear instabilities associated with the along-front shear are not resolved in the two-dimensional simulations.

gradient matching the initial condition. The simulations use a staggered grid with 1024×200 gridpoints in the y and z directions with uniform resolution. Details of the numerical method can be found in Taylor (2008).

3.2. *Results*

Figure 4(*a*) shows time series of the perturbation kinetic energy, k, for all five cases listed in table 1. For comparison with the numerical simulations (solid lines), results from a viscous version of the analysis presented in § 2.2 are shown as dashed lines, using the same Reynolds and Péclet numbers as in the simulations. To avoid a brief spin-up period in the simulations, and to focus on the most unstable modes, results are shown starting at 5 inertial periods. In general, the agreement between the simulations and theory is very good. The somewhat slower growth seen in the simulations appears to be primarily due to the finite vertical extent in the simulations and boundary effects. The strong dependence on the phase of the inertial shear is particularly striking. When the inertial shear is down-front at $t = 0$ ($Ri = 1.91$, $\phi = 0$, blue curves), the perturbation kinetic energy grows by more than three orders of magnitude over four inertial periods. In contrast, when the inertial shear is up-front at $t = 0$ ($Ri = 1.91$, $\phi = \pi$, magenta curves), the perturbation kinetic energy decreases, albeit slowly. The difference between the simulations and theory in this latter case

stems from the fact that the simulations started with a broad range of wavenumbers, several of which decay slowly, while the dashed curve for the theory shows only the single, most slowly decaying mode.

As predicted by the theory, the primary energy source of the simulated instability is the inertial shear via the ageostrophic shear production (*AGSP*, see (2.24)). Figure 4(*b*) shows the evolution of the mean depth-dependent ageostrophic kinetic energy (K) with $Ri = 1.91$ and $\phi = 0$ (black line). Here, K is calculated using the mean velocity after removing the thermal wind shear and the depth-averaged mean flow: $K = (1/2)\boldsymbol{v}_s \cdot \boldsymbol{v}_s$ where $\boldsymbol{v}_s = \overline{\boldsymbol{u} - \langle \boldsymbol{u} \rangle} - S^2 z/f\hat{\boldsymbol{x}}$ is the mean velocity associated with the ageostrophic shear and the angular brackets denote a depth average. The linear phase of the instability, with exponentially growing perturbations continues until about 15 inertial periods. At this point, the instability becomes finite-amplitude, nonlinear, and unstable to a secondary shear instability with the across-front shear causing the gradient Richardson number to drop below 0.25 at many points in the domain (see figure 4*b*, dots). The decrease in ageostrophic kinetic energy, K, is almost entirely balanced by an increase in the time-integrated *AGSP* (blue line). The *AGSP* transfers energy from the mean shear into the perturbation kinetic energy (k), but only a relatively small fraction of this energy remains stored in k. Most of the remainder is either lost through viscous dissipation or is used to raise the centre of gravity of the fluid by mixing the stable stratification.

The terms in the perturbation kinetic energy budget are shown in figure 5(*b*) for the simulations (solid lines) and the theory (dashed lines), for two inertial periods during the linear phase of the instability with $Ri = 1.91$ and $\phi = 0$. For reference, the time-series of the domain-averaged buoyancy frequency $\overline{N}$ is shown in figure 5(*a*). To more easily compare changes in the kinetic energy during this phase of rapid exponential growth, each term in the budget has been divided by k. Again, the agreement between the theory and simulations is excellent. Consistent with figure 4(*b*), when integrated over a full inertial period, the *AGSP* is the dominant source of kinetic energy. However, the geostrophic shear production (*GSP*) is of a similar magnitude, which results in a significant shift of the phase of the maximum growth rate and negative growth rates during the weakly stratified phase of the inertial cycle.

Figure 6 shows the cross-front velocity (colour shading) and isopycnals (white contours) at several times during the simulation with $Ri = 1.91$ and $\phi = 0$. The left and right columns correspond to times with maximum and minimum stratification, respectively. Figure 6(*a*) shows the flow during the early (linear) phase with exponential growth. Although the simulations are not constrained to have a particular perturbation slope, the most rapidly growing motions are closely aligned with the isopycnals throughout the inertial cycle, consistent with the assumption made in the stability analysis. The along-isopycnal velocity bands are associated with strong vertical shear, and as the unstable mode grows in amplitude, it eventually becomes unstable to a secondary shear instability with $Ri_g = N^2/(\partial v/\partial z)^2 < 0.25$, as indicated in figure 4(*b*). Figure 6(*b*) shows the flow just after the onset of this shear instability (left), and a half-inertial period later (right). At $tf/(2\pi) = 16$, small Kelvin–Helmholtz billows are visible between the alternating bands of cross-front velocity. This is highly reminiscent of the secondary shear instability that equilibrates symmetric instability (Taylor & Ferrari 2009). By $tf/(2\pi) = 16.5$, the resulting turbulence and down-scale energy transfer has significantly decreased the energy associated with the primary parametric subharmonic instability, leaving a larger-scale mode behind.

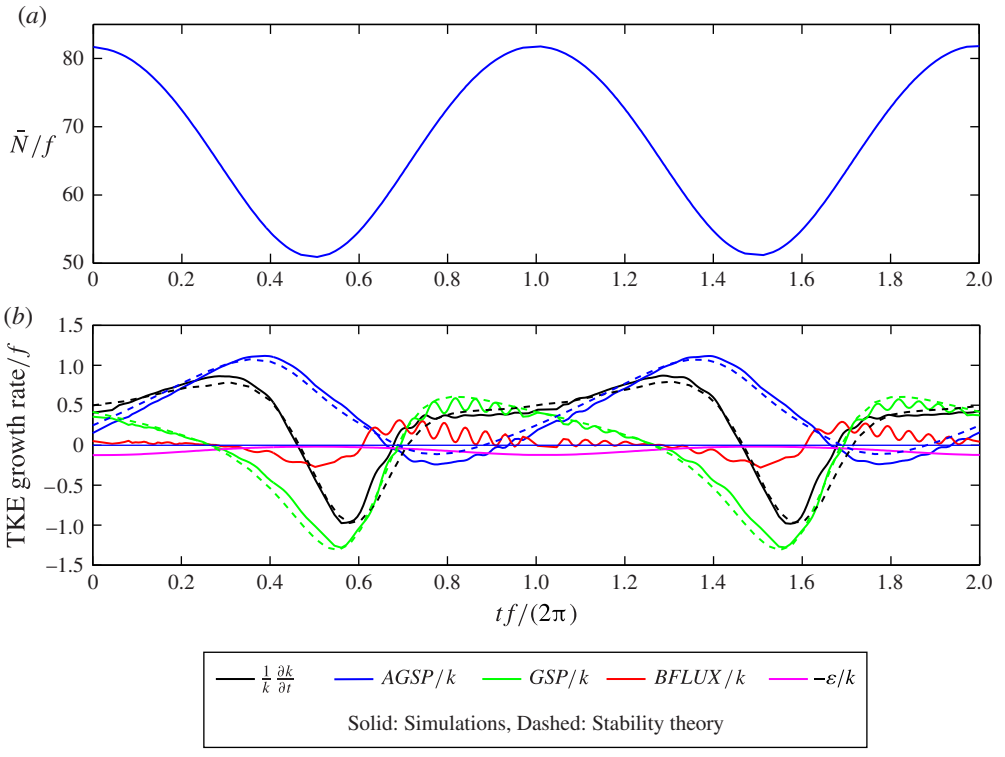

FIGURE 5. Time series showing (*a*) two inertial periods of the domain-averaged buoyancy frequency and (*b*) the terms in the turbulent kinetic energy budget, where ε is the dissipation of kinetic energy.

4. Discussion and conclusion

We have discovered a parametric subharmonic instability that can damp inertial waves locally as opposed to remotely (i.e. after propagation to lower latitudes, (e.g. Nagasawa *et al.* 2000)). For the instability to develop, both inertial and thermal wind shear must be present, since the latter can lower the minimum frequency of inertia–gravity waves (1.1) to a subharmonic of the inertial frequency. The instability is predicted to form when the Richardson number of the geostrophic flow nears a critical value, Ri_{PSI} (2.15), which is a function of the initial value of the inertial shear.

A stability analysis involving plane-wave perturbations with streamlines parallel to isopycnals confirms this prediction and elucidates the growth mechanism of the instability. The parametric subharmonic instability extracts kinetic energy from the inertial motion through shear production associated with wave momentum fluxes. While the ageostrophic shear changes sign during the inertial cycle, the wave momentum flux is of a single sign determined by the isopycnal slope. In spite of the variable shear, the growing perturbations are able to maximize shear production by modulating the amplitude of the momentum flux so that it is strongest (weakest) when the momentum flux is directed down (up) the gradient in momentum of the inertial current. This requires a particular phase relation between the perturbation and inertial motion that can be attained when the frequency of the perturbation inertia–gravity wave is a subharmonic of the inertial frequency, hence the parametric subharmonic instability.

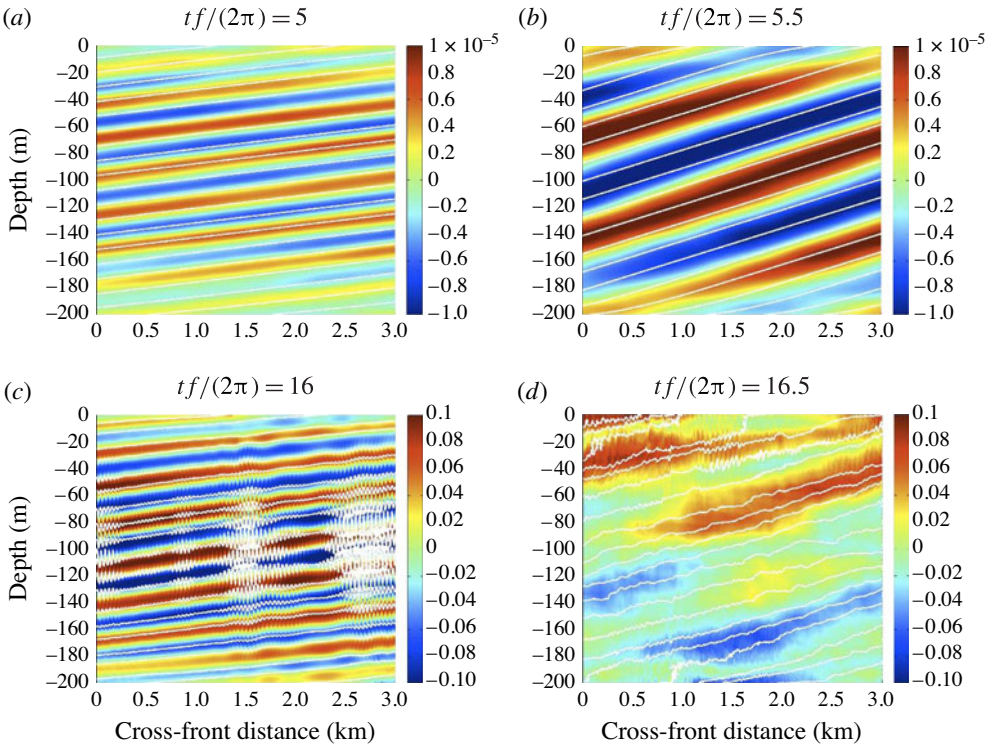

FIGURE 6. Visualizations of the cross-front velocity (colour shading) and isopycnals (white contours) from the numerical simulation highlighted in bold in table 1. (*a*) A time during the linear phase of the instability, with nearly along-isopycnal motion, and at times of maximum (left) and minimum (right) stratification. (*b*) Again times corresponding to minimum and maximum stratification, but now at a later time immediately following the onset of a secondary shear instability.

Numerical simulations initialized with random noise rather than plane waves develop a growing mode with phase lines parallel to isopycnals when the instability criterion is satisfied in accordance with the theory. The growing parametric subharmonic instability damps the inertial motion at rates in agreement with the stability analysis, but when it reaches finite amplitude it develops secondary shear instabilities that dissipate its kinetic energy and mix density. We would like to emphasize that these shear instabilities would not form in the absence of the parametric subharmonic instability because the minimum Richardson numbers of the combined geostrophic and inertial motions considered here are above the criterion for Kelvin–Helmholtz instability (the gradient Richardson number is greater than $1/4$ everywhere in the flow). By enhancing the vertical shear, the growth of the parametric subharmonic instability lowers the gradient Richardson number to subcritical values, thereby opening a pathway to turbulence where kinetic energy in inertial motions is transferred to small scales and dissipated.

Where might this form of parametric subharmonic instability occur in the ocean? The instability requires a baroclinic, geostrophic current and hence a horizontal buoyancy gradient. Such gradients are concentrated at ocean fronts, which are a ubiquitous feature of the upper ocean as evidenced by the observed, near universal

-2 scaling law for the slope of horizontal wavenumber spectra of buoyancy in the mixed layer (e.g. Fox-Kemper *et al.* 2011, and references therein). Thus thermal wind shear is found throughout the upper ocean. However, for the parametric subharmonic instability to develop the thermal wind shear must be accompanied by relatively weak, but non-zero, stratification so that the Richardson number of the geostrophic flow satisfies the instability criterion (2.15). Such conditions are likely to be found beneath the surface mixed layer and above the strongly stratified pycnocline. It is precisely in this region where inertial shears are observed to be strongest and where much of the near-surface dissipation of inertial motions is thought to occur (Plueddemann & Farrar 2006), and it is possible that the parametric subharmonic instability described here contributes to this dissipation. However, to investigate this possibility more fully, the effects on the instability of spatially-varying stratification and shear, and the presence of a boundary should be studied.

In addition, it would be of interest to extend the analysis to fully three-dimensional disturbances as it may yield a richer set of instabilities. For example, it is known that oscillatory, sheared equatorial flows develop two-dimensional parametric subharmonic instabilities that feed off of inertial motions (e.g. d'Orgeville & Hua 2005) as well as three-dimensional instabilities that involve resonant interactions of inertia–gravity, Kelvin and Rossby waves (Natarov & Richards 2009). While Kelvin and Rossby waves are absent in the mid-latitude, open-ocean, f-plane applications considered here, it is possible that edge waves that form in the presence of a horizontal density gradient and a boundary could resonantly interact with inertia–gravity waves and result in analogous three-dimensional instabilities.

To conclude we would like to comment on the dependence of the instability criterion (2.15) on the initial direction of the inertial shear. This dependence arises because the inertial shear modulates the potential vorticity. Although built into the initial conditions of our simplified model, in reality the potential vorticity of the flow is set by frictional or diabatic processes. Frictional forces associated with winds are particularly effective at modifying the potential vorticity of baroclinic currents for certain wind directions (e.g. Thomas 2005), and if these forces are temporally variable, they can generate inertial motions as well. Therefore, at wind-forced fronts the development of parametric subharmonic instability will probably depend on the wind's direction relative to the front and its time history. Fleshing out this story and understanding the dynamics of parametric subharmonic instability at a front actively forced by winds will be the subject of a future study.

Acknowledgements

This work was supported by the Office of Naval Research grant N00014-09-1-0202. LT received additional support from the National Science Foundation award OCE-1260312.

REFERENCES

ALFORD, M. & GREGG, M. 2001 Near-inertial mixing: Modulation of shear, strain and microstructure at low latitude. *J. Geophys. Res.* **106**, 16947–16968.

CRAIK, A. D. D. 1989 The stability of unbounded two- and three-dimensional flows subject to body forces: some exact solutions. *J. Fluid Mech.* **198**, 275–292.

FERRARI, R. & WUNSCH, C. 2009 Ocean circulation kinetic energy: Reservoirs, sources, and sinks. *Annu. Rev. Fluid Mech.* **41**, 253–282.

FOX-KEMPER, B., DANABASOGLU, G., FERRARI, R., GRIFFIES, S. M., HALLBERG, R. W., HOLLAND, M. M., MALTRUD, M. E., PEACOCK, S. & SAMUELS, B. L. 2011 Parameterization of mixed layer eddies. III: Implementation and impact in global ocean climate simulations. *Ocean Model.* **39**, 61–78.

HOSKINS, B. J. 1974 The role of potential vorticity in symmetric stability and instability. *Q. J. R. Meteorol. Soc.* **100**, 480–482.

HOSKINS, B. J. 1982 The mathematical theory of frontogenesis. *Annu. Rev. Fluid Mech.* **14**, 131–151.

KUNZE, E., SCHMITT, R. W. & TOOLE, J. M. 1995 The energy balance in a warm-core ring's near-inertial critical layer. *J. Phys. Oceanogr.* **25**, 942–957.

MÜLLER, P., HOLLOWAY, G., HENYEY, F. & POMPHREY, N. 1986 Nonlinear interactions among internal gravity waves. *Rev. Geophys.* **24**, 493–536.

NAGASAWA, M., NIWA, Y. & HIBIYA, T. 2000 Spatial and temporal distribution of the wind-induced internal wave energy available for deep water mixing in the North Pacific. *J. Geophys. Res.* **105**, 13933–13943.

NATAROV, A. & RICHARDS, K. J. 2009 Three-dimensional instabilities of oscillatory equatorial zonal shear flows. *J. Fluid Mech.* **623**, 59–74.

D'ORGEVILLE, M. & HUA, B. L. 2005 Equatorial inertial-parametric instability of zonally symmetric oscillating shear flows. *J. Fluid Mech.* **531**, 261–291.

PLUEDDEMANN, A. J. & FARRAR, J. T. 2006 Observations and models of the energy flux from the wind to mixed-layer inertial currents. *Deep-Sea Res.* II **53**, 5–30.

TAYLOR, J. R. 2008 Numerical simulations of the stratified oceanic bottom boundary layer. PhD thesis, University of California, San Diego.

TAYLOR, J. & FERRARI, R. 2009 The role of secondary shear instabilities in the equilibration of symmetric instability. *J. Fluid Mech.* **622**, 103–113.

TAYLOR, J. & FERRARI, R. 2010 Buoyancy and wind-driven convection at a mixed-layer density front. *J. Phys. Oceanogr.* **40**, 1222–1242.

THOMAS, L. N. 2005 Destruction of potential vorticity by winds. *J. Phys. Oceanogr.* **35**, 2457–2466.

THOMAS, L. N. & TAYLOR, J. R. 2010 Reduction of the usable wind-work on the general circulation by forced symmetric instability. *Geophys. Res. Lett.* **37**, L18606.

WHITT, D. B. & THOMAS, L. N. 2013 Near-inertial waves in strongly baroclinic currents. *J. Phys. Oceanogr.* **43**, 706–725.